Linear Perturbation Amplification in Self-Similar Ablation Flows of ICF

Florian Abéguilé*, Carine Boudesocque-Dubois†, Jean-Marie Clarisse† and Serge Gauthier†

∗ CPHT, Ecole Polytechnique, 91128, Palaiseau Cedex, FRANCE
† CEA Bruyères-le-Châtel, B.P. 12, 91680 Bruyères-le-Châtel, FRANCE

ABSTRACT

The stability of an ablative flow is of importance in inertial confinement fusion (ICF). Here, we exhibit a family of exact self-similar solutions of the gas dynamics equations with nonlinear heat conduction for semi-infinite slabs of perfect gases. Such self-similar solutions which arise for particular but realistic initial and boundary conditions—boundary pressure and incoming heat flux follow time power laws—are representative of the early stage of the ablation of a pellet by a laser, where a shock wave propagates upstream of a thermal front. Following the work of Boudesocque-Dubois *et al.* [1, 2], these solutions are computed using a dynamical multidomain Chebyshev pseudo-spectral method [3]. A wide variety of ablation configurations may thus be obtained. Linear stability analyses of such time-dependent solutions are performed by solving an initial and boundary value problem for linear perturbations. The numerical methods are based on a dynamical multidomain Chebyshev pseudo-spectral method and an operator splitting between a hyperbolic system and a parabolic equation. Here, focusing on the laser imprint problem, we have considered boundary heat flux perturbations and obtained space-time evolutions of flow perturbations for a wide range of wavenumbers. By contrast with steady low Mach number models of ablation front instabilities, we obtain that: (a) maximum perturbation amplitudes in the thin ablation layer are reached for transverse wavenumber $k_\perp = 0$, (b) the damping of ablation front perturbations is closely related to thermal diffusion, (c) ablation front perturbations seem to persist although the transverse wave number increases, (d) a complex wave-like structure arises between the ablation front and the shock-wave front.

1 INTRODUCTION

Self-similar solutions have been the object of continuing interest in fluid mechanics [4, 5, 6]. In addition to providing insights in complex hydrodynamic phenomena, through useful scaling relationships, and enabling qualitative and parametric studies in realistic configurations, they have been profitably used for hydrodynamic stability analyses beyond the uniform or steady flow assumptions [7, 8]. Hydrodynamic instabilities are a key issue in laser-driven inertial confinement fusion (ICF) where thermonuclear burn is expected to be achieved for a sufficiently symmetric implosion of a spherical capsule [9]. Implosions of such capsules which, for the simplest designs, consist of an optically-thick shell coated on the inside with solid, cryogenic deuterium-tritium fuel, are highly nonuniform and unsteady complex flows. These features and the variety of hydrodynamic instability phenomena which may be triggered during these implosions render any stability analysis of such flows particularly arduous. For these reasons most of the works devoted to this subject have focused on the kinds of instabilities which are thought to be the most

*E-mail: abeguile@cpht.polytechnique.fr
†E-mail: carine.boudesocque@cea.fr, jean-marie.clarisse@cea.fr and serge.gauthier@cea.fr

detrimental to the pellet thermonuclear yield. Among those, the so-called ablative Rayleigh-Taylor instability [10, 11, 12], which occurs during the shell acceleration phase [9], has received much attention since the late 1970's. Hence numerous analytical models—established in slab symmetry, for a steady mean flow of infinite extent, a uniform and constant inertial force field, continuous or discontinuous ablation profiles as well as other, more or less restrictive, assumptions (*e. g.* incompressible or isobaric approximations)—have been proposed for the linear regime of this instability [10, 13, 14, 15, 16, 17, 18, 19, 20, 21, 22, 23]. Such models, within the scope delimited by their assumptions, have undoubtedly contributed to a better understanding of the rather complex planar ablation front instability in its linear regime. Being analytical, they fail however to render some of the critical features of actual ICF implosions such as convergence or unsteadiness effects. The early stage of the capsule irradiation—the so-called "shock-transit phase"—is a configuration where mean flow unsteadiness should not be underestimated. Indeed, numerical simulations indicate that the mean flow profiles resulting from the propagation, in the deflagration regime, of the thermal wave-front are more akin to self-similar flows than to steady states [24]. A proper treatment of this phase of the implosion is of uttermost importance as perturbation growths at the ablation front and at the fore-running shock-wave front will determine the subsequent developments of instabilities throughout the whole shell. Different factors—initial ablator surface-finish defects, irradiation non uniformities—which cannot be completely eliminated, are at the origin of such perturbations. Existing models for perturbation growth [25, 26, 24, 27, 28] during this shock-transit phase make use of a linear gasdynamic model for a uniform convective mean flow with boundary conditions given by, on one end, the Rankine-Hugoniot relations for a rippled planar shock front, and, on the other end, jump conditions for a perturbed discontinuous ablation front. Here, we present a totally different approach based on exact self-similar solutions for semi-infinite planar ablation flows in the deflagration regime [29, 30, 31, 32, 33, 34, 35, 36, 1, 2, 37]. Such solutions describe the whole flow region spanning the upstream fluid at rest, the shock-wave front, the compressed region, the thermal front and the heat conducting region up to the material plane where the incoming heat flux is applied. Radiative or electronic heat conduction may equally be considered. The complexity of the system of ordinary differential equations (ODEs) to be solved for requires us to have recourse to numerical integration in obtaining these solutions. Consequently, the problem of instability growth is addressed by solving initial and boundary value problems (IBVPs) for three-dimensional linear perturbations. By doing so we ensure that both the continuous and unsteady features of ablation flows are fully taken into account.

2 MEAN FLOW

We consider a semi-infinite slab ($x \geq 0$) of a perfect gas, initially at rest, subject to an external heat flux imposed at the boundary $x = 0$.

2.1 EQUATIONS AND BOUNDARY CONDITIONS

The hydrodynamic equations for a one-dimensional flow in planar symmetry are written in terms of the Lagrangian variable m such that $\mathrm{d}m = \overline{\rho}\,\mathrm{d}x$, as

$$\begin{aligned} &\frac{\partial}{\partial t}\left(\frac{1}{\overline{\rho}}\right) - \frac{\partial \overline{v}_{_x}}{\partial m} = 0, \\ &\frac{\partial \overline{v}_{_x}}{\partial t} + \frac{\partial \overline{p}}{\partial m} = 0, \\ &\frac{\partial}{\partial t}\left(\frac{1}{2}\overline{v}_{_x}^{\,2} + \overline{\mathcal{E}}\right) + \frac{\partial}{\partial m}\left(\overline{p}\,\overline{v}_{_x} + \overline{\varphi}_{_x}\right) = 0, \end{aligned} \tag{1}$$

with the nonlinear heat flux :

$$\overline{\varphi}_{_x} = -\chi\,\overline{\rho}^{1+\mu}\,\overline{T}^{\nu}\,\frac{\partial \overline{T}}{\partial m}, \tag{2}$$

where χ is the thermal conductivity coefficient and μ and ν depend on the interaction process between the incident energy and the fluid under consideration. System (1) is completed by the perfect gas equation of state $\overline{p} = \overline{\rho}\,R\,\overline{T}$.

In these equations, $\overline{\rho}$ denotes the density, $\overline{v}_x$ the longitudinal velocity, $\overline{p}$ the pressure, $\overline{T}$ the temperature, R the perfect gas constant and $\overline{\mathcal{E}}$ the specific internal energy. Choosing a system of units based on χ, R, the initial density $\rho_{\rm i}$ and a reference time t_*, the nonlinear heat flux and the equation of state read

$$\overline{\varphi}_x \;=\; -\,\overline{\rho}^{1+\mu}\,\overline{T}^{\nu}\,\frac{\partial \overline{T}}{\partial m}, \tag{3}$$

$$\overline{p} \;=\; \overline{\rho}\,\overline{T}, \tag{4}$$

while system (1) is left unchanged. At the initial time $t_{\rm i}=0$, the fluid of uniform density $\overline{\rho}_{\rm i}$ is at rest and is assumed to occupy the half-space $x \geq 0$. For initial conditions

$$\begin{aligned} \overline{\rho}(m,0) &= 1, \\ \overline{v}_x(m,0) &= 0, \quad \text{for } m \geq 0, \\ \overline{T}(m,0) &= 0, \end{aligned} \tag{5}$$

and boundary conditions of the form

$$\begin{aligned} \overline{p}(0,t) &= \overline{p}_*\,(t/t_*)^{2(\alpha-1)}, \\ \overline{\varphi}_x(0,t) &= \overline{\varphi}_*\,(t/t_*)^{3(\alpha-1)}, \end{aligned} \tag{6}$$

where $\alpha = (2\nu-1)/(2\nu-2)$, system (1) admits self-similar solutions [31, 35] in terms of the variable $\xi = m/t^{\alpha}$. Here, $\overline{p}_*$ and $\overline{\varphi}_*$ are some characteristic values of the pressure and heat flux, respectively. Other sets of initial and boundary conditions could as well be considered [31]. Introducing the time power-law dependencies for the physical variables

$$\begin{aligned} \overline{\rho}(m,\,t) &= \qquad\;\; \overline{G}(\xi), \\ \overline{v}_x(m,\,t) &= t^{\alpha-1} \;\; \overline{V}_x(\xi), \\ \overline{T}(m,\,t) &= t^{2(\alpha-1)} \;\; \overline{\Theta}(\xi), \\ \overline{\varphi}_x(m,\,t) &= t^{3(\alpha-1)} \;\; \overline{\Phi}_x(\xi), \end{aligned} \tag{7}$$

equations (1) and (3) reduce to a system of ODEs:

$$\frac{\mathrm{d}\,\mathbf{Y}}{\mathrm{d}\xi} = \boldsymbol{\mathcal{F}}(\xi,\mathbf{Y}), \tag{8}$$

in terms of the reduced function vector $\mathbf{Y}^{\mathsf{T}} = (\overline{G}\;\overline{V}_x\;\overline{\Theta}\;\overline{\Phi}_x)$. The components $\mathcal{F}_i$ of the vector $\boldsymbol{\mathcal{F}}$ are given by

$$\begin{gathered} \mathcal{F}_1 = \overline{G}^{\,2}\,N/D, \quad \mathcal{F}_2 = \alpha\,\xi\,N/D, \quad \mathcal{F}_3 = F, \\ \mathcal{F}_4 = \left(\alpha\,\xi F - 2(\alpha-1)\overline{\Theta}\right)/(\gamma-1) - \alpha\xi\,\overline{G\Theta}\,N/D, \end{gathered} \tag{9}$$

where γ denotes the fluid adiabatic exponent and

$$\begin{aligned} N &= (\alpha-1)\overline{V}_x + \overline{G}\,F, \\ D &= \alpha^2\,\xi^2 - \overline{G}^{\,2}\,\overline{\Theta} \quad \text{and} \quad F = -\overline{\Phi}_x\,\overline{G}^{\,-\mu-1}\,\overline{\Theta}^{\,-\nu}. \end{aligned} \tag{10}$$

In the limit $m \to +\infty$, system (8) has the following solution: $\overline{G}=1$ and $\overline{V}_x = \overline{\Theta} = 0$. At the origin, Eqs.(6) read

$$\begin{aligned} \left(\overline{G\Theta}\right)(\xi=0) &= \mathcal{B}_p, \\ \overline{\Phi}_x(\xi=0) &= \mathcal{B}_\varphi, \end{aligned} \tag{11}$$

where $\mathcal{B}_p$ and $\mathcal{B}_\varphi$ are dimensionless numbers based on $\overline{p}_*$ and $\overline{\varphi}_*$, respectively.

2.2 NUMERICAL METHOD

System (8) does not seem to admit analytical solutions and it turns out that this system of ODEs with boundary conditions (5)-(6) requires a rather sophisticated numerical integration method. The problem raised by the presence of the singularity $D = 0$ may be circumvented by introducing a shock wave discontinuity at an arbitrary point, say ξ_s. However, due to the presence of a thermal conductivity, this shock wave has a non-zero thickness [38] which we neglect here—the sole approximation made in computing these self-similar solutions. As suggested in [32, 33, 34, 17], the domain $[0, \xi_s]$ may be decomposed into two regions: *(i)* a region, downstrean of the shock-wave front ($\xi_f < \xi_s$), where convection is dominant and *(ii)* a region, corresponding to the vicinity of the origin where the external heat flux is applied, for which heat conduction is important. Consequently, the system of ODEs to be considered on the domain (ξ_f, ξ_s) is (8) without heat conduction. The five-stage numerical method we devised may be summarized as follows:

1 *Backward finite-difference integration* Using a sixth-order adaptive-step Runge-Kutta scheme, system (8) without heat conduction is first integrated from ξ_s^- to ξ_f^+, followed by an integration of system (8) from ξ_f^- to 0. At the end of this shooting process, we obtain a first estimate of $\mathbf{Y}(0)$ in agreement with the boundary conditions (11).

2 *Forward finite-difference integration* System (8) is forward-integrated with the above Runge-Kutta scheme, from 0 up to a certain point ξ_{so}. This point ξ_{so} is adjusted to provide the best approximation of the Rankine-Hugoniot relations. The resulting value of ξ_{so} defines a new value for the shock-wave location ξ_s.

3 *Forward finite-difference integration on a multidomain spectral grid* We use the dynamical multidomain collocation spectral method described in [39, 40, 41].

4 *Relaxation process* We now apply a relaxation method to system (8) with a spectral preconditionning [42]. At the end of this process, we obtain a good approximation of the solution: the relative error is close to machine precision, except around the subdomain interfaces where the error depends on the steepness of the solution but always remains low.

5 *Boundary condition adjustment* In order to improve the approximation of the Rankine-Hugoniot relations, we have recourse to a recursive process for modifying the boundary condition value at the origin. This iterative process allows us to gain one order of magnitude on the error at ξ_s. This residual error is in fact related to the thickness of the isothermal shock wave.

2.3 RESULTS

The mean flow solutions depend on five dimensionless parameters: the two exponents μ and ν of the heat conductivity coefficient (3), and the three dimensionless numbers γ, $\mathcal{B}_p$ and $\mathcal{B}_\varphi$. Choosing to model a mono-atomic gas ($\gamma = 5/3$), and an electronic thermal conduction ($\mu = 0$ and $\nu = 5/2$), we present numerical results for three different choices of ($\mathcal{B}_p$, $\mathcal{B}_\varphi$) (see Table 1). The first two configurations (I and II) have been obtained from a numerical simulation of the ablation of a planar foil under Mégajoule laser conditions whereas the last one is a variation about the corresponding values of ($\mathcal{B}_p$, $\mathcal{B}_\varphi$). For electronic thermal conduction, the exponent of the self-similar variable α evaluates to 4/3 and the time power-law dependencies for the physical variables become:

$$\begin{aligned}
\overline{\rho}(m,\,t) &= \overline{G}(\xi),\\
\overline{v}_{_x}(m,\,t) &= t^{1/3}\ \overline{V}_{_x}(\xi),\\
\overline{T}(m,\,t) &= t^{2/3}\ \overline{\Theta}(\xi),\\
\overline{\varphi}_{_x}(m,\,t) &= t\ \overline{\Phi}_{_x}(\xi),\\
\overline{a}(m,\,t) &= t^{-2/3}\ \overline{A}(\xi),
\end{aligned} \tag{12}$$

where $\overline{a}(m,\, t)$ denotes the fluid particle acceleration with $\overline{A}$, the corresponding reduced function. Note that the heat flux increases linearly in time, the velocity like $t^{1/3}$ while the acceleration decreases like $t^{-2/3}$.

	$\mathcal{B}_p\,(10^{-2})$	$\mathcal{B}_\varphi\,(10^{-2})$	$\xi_a\,(10^{-1})$	$\xi_c\,(10^{-1})$
I	0.1	2.6	1.25	3.00
II	3.0	25.7	0.23	1.10
III	0.1	0.1	0.95	2.72

Table 1: Parameters of simulations for three different choices of ($\mathcal{B}_p$, $\mathcal{B}_\varphi$).

The profiles of the reduced functions for densities, velocities, temperatures and pressures are given in Fig. 1. One can distinguish four zones : *(1)* a low density region (with a high temperature) between the origin and the ablation front, *(2)* a thin layer corresponding to continuous thermal front, *(3)* a cold and quasi-isothermal region where the density decreases slightly and the velocity is almost constant and *(4)* a region upstream of the shock wave where the fluid is at rest and the temperature zero as it is required by the self-similarity analysis. Note that configurations I and II are heat-flux dominated while configuration III is neither heat-flux nor pressure dominated. For this last case, the velocity of the expanding plasma, usually referred to as "blow-off velocity", is very small compared to the other two cases.

The location of the ablation front ξ_a is here defined by the maximum of the density. A characteristic length of

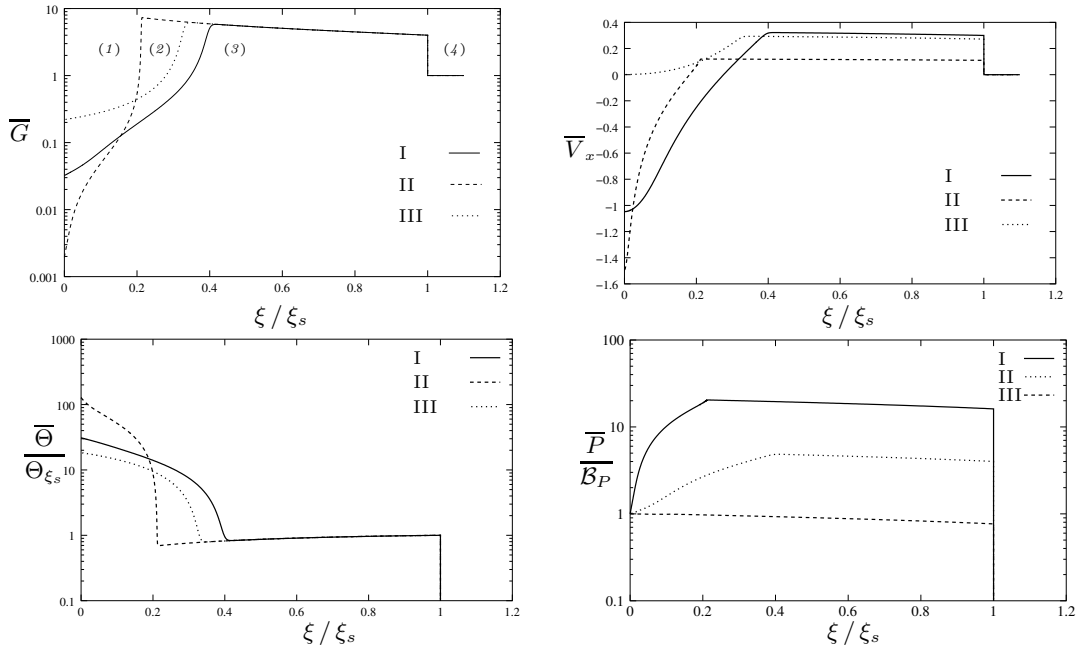

Figure 1: Spatial profiles in the ξ-variable normalized to ξ_s of the reduced functions for the density (top left), velocity (top right), temperature normalized to the temperature at the shock wave (bottom left) and pressure normalized to the pressure at the origin (bottom right) for three different choices of ($\mathcal{B}_p$, $\mathcal{B}_\varphi$) (see Table 1).

this ablation front region may be given by the density gradient length scale [15], here

$$l_{ABLA} \,=\, \min\left[\left(\frac{1}{\rho}\frac{\partial\rho}{\partial x}\right)^{-1}\right] \,=\, t^{4/3}\,\min\left[\left(\frac{\mathrm{d}\overline{G}}{\mathrm{d}\xi}\right)^{-1}\right] \,=\, t^{4/3}\,L_{ABLA}. \tag{13}$$

In this formula, L_{ABLA} is a reduced function of a length. We can define other characteristic lengths, like the total length of the flow l_{TOT} as

$$l_{TOT} \,=\, |x\,(\xi_s) - x\,(0)\,| \,=\, t^{4/3}\,L_{TOT}, \tag{14}$$

and the length of the heat-conduction zone as

$$l_{COND} \,=\, |x\,(\xi_a) - x\,(0)\,| \,=\, t^{4/3}\,L_{COND}. \tag{15}$$

A necessary instability criterion for compressible fluids [38, 43] which, written in terms of the ξ-variable, reads

$$\overline{G}^2 \left(\frac{\mathrm{d}\overline{G}}{\mathrm{d}\xi} - \frac{1}{\gamma\overline{\Theta}} \frac{\mathrm{d}\overline{P}}{\mathrm{d}\xi} \right) \frac{\mathrm{d}\overline{P}}{\mathrm{d}\xi}\, t^{-2} \,<\, 0, \tag{16}$$

may also be used to define another characteristic length, namely the length of the zone $[\xi_{inf}, \xi_{sup}]$ where it is satisfied

$$l_{INS} \,=\, |x\,(\xi_{sup}) - x\,(\xi_{inf})\,| \,=\, t^{4/3}\,L_{INS}. \tag{17}$$

The velocity $\overline{w}$ of a point of fixed abscissa ξ is given by

$$\overline{w}(\xi,\, t) \,=\, t^{1/3} \left(\frac{4\,\xi}{3\,\overline{G}\,(\xi)} \,+\, \overline{V}_{_x}\,(\xi) \right), \tag{18}$$

which by integration gives the physical abscissa x at this point

$$x\,(\xi,\, t) \,=\, t^{4/3} \left[\left(\frac{\xi}{\overline{G}\,(\xi)} \,+\, \frac{3}{4} \overline{V}_{_x}\,(\xi) \right) \right] \,+\, \text{cst.} \tag{19}$$

The material velocity relative to the ablation front is given by

$$\overline{u}(\xi,\, t) \,=\, \overline{v}_{_x}(\xi,\, t) - \overline{w}(\xi_a,\, t) \,=\, t^{1/3} \left(\overline{V}_{_x}(\xi) \,-\, \overline{V}_{_x}(\xi_a) - \frac{4\,\xi_a}{3\,\overline{G}(\xi_a)} \right) = t^{1/3}\,\overline{U}(\xi), \tag{20}$$

so that, the ablation velocity is simply

$$\overline{u}_{_a}(t) = -t^{1/3}\,\frac{4\,\xi_a}{3\,\overline{G}(\xi_a)} = -t^{1/3}\,\overline{U}(\xi_a). \tag{21}$$

Self-similar ablation fronts are usually characterized by three dimensionless parameters: a Mach number M, a Froude number Fr and a Péclet number Pe. Here, all these dimensionless numbers are expressed in terms of the material velocity relative to the ablation front. In particular, the Mach number at the ablation front is defined as the isothermal Mach number, or

$$\mathsf{M}_a \,=\, \frac{|\overline{U}(\xi_a)|}{\sqrt{\overline{P}(\xi_a)/\overline{G}(\xi_a)}}, \tag{22}$$

the Froude number as

$$\mathsf{Fr}_a \,=\, \frac{|\overline{U}(\xi_a)|}{\sqrt{\overline{A}_{_a}(\xi_a)\,L_{ABLA}}} \tag{23}$$

and the Péclet number as

$$\mathsf{Pe}_a \,=\, \frac{\gamma}{\gamma-1} \frac{L_{TOT}\overline{G}^2(\xi_a)\,|\overline{U}(\xi_a)|}{\overline{\Theta}^{5/2}(\xi_a)}. \tag{24}$$

The structure, in physical space, of the mean flow for configuration I is illustrated in Fig. 2 under the form of x-coordinate profiles taken at three different times. Note that the profiles of the variables in physical space are different from the profiles of the reduced functions. Among these differences, the profile of the density in physical space is much steeper than that of its reduced function. In particular, the compressed region is small compared to the blow-off region, whereas these two thicknesses are comparable in terms of reduced functions (see Fig. 1 and Fig. 2). Here, the low Mach number approximation used in other studies [15, 17] seems to be justified in view of the weak value of the parameter $\mathsf{M}_a^2/\mathsf{Fr}_a$ (see Table 2). But, thanks to our model we will be able to study the influence of acoustic waves on the flow stability. By varying the parameters $(\mathcal{B}_p,\, \mathcal{B}_\varphi)$, we may obtain a wide range of profiles. At this point, the numerical method described in this paper has successfully performed on given realistic profiles.

	L_{TOT}	L_{CON}	$L_{ABL}\,(10^{-3})$	$L_{INS}\,(10^{-3})$	$\overline{U}_a\,(10^{-2})$	$\mathsf{M}_a\,(10^{-1})$	Fr_a	$\mathsf{Pe}_a\,(10^5)$
I	1.23	1.21	0.04	0.02	-0.43	0.63	10.68	0.31
II	1.08	1.05	1.80	0.82	-2.87	1.39	3.88	0.22
III	0.27	0.23	1.30	0.49	-2.03	1.08	2.94	0.98

Table 2: Characteristic lengths, ablation velocity and dimensionless numbers for the three different choices of ($\mathcal{B}_p$, $\mathcal{B}_\varphi$) found in Table 1.

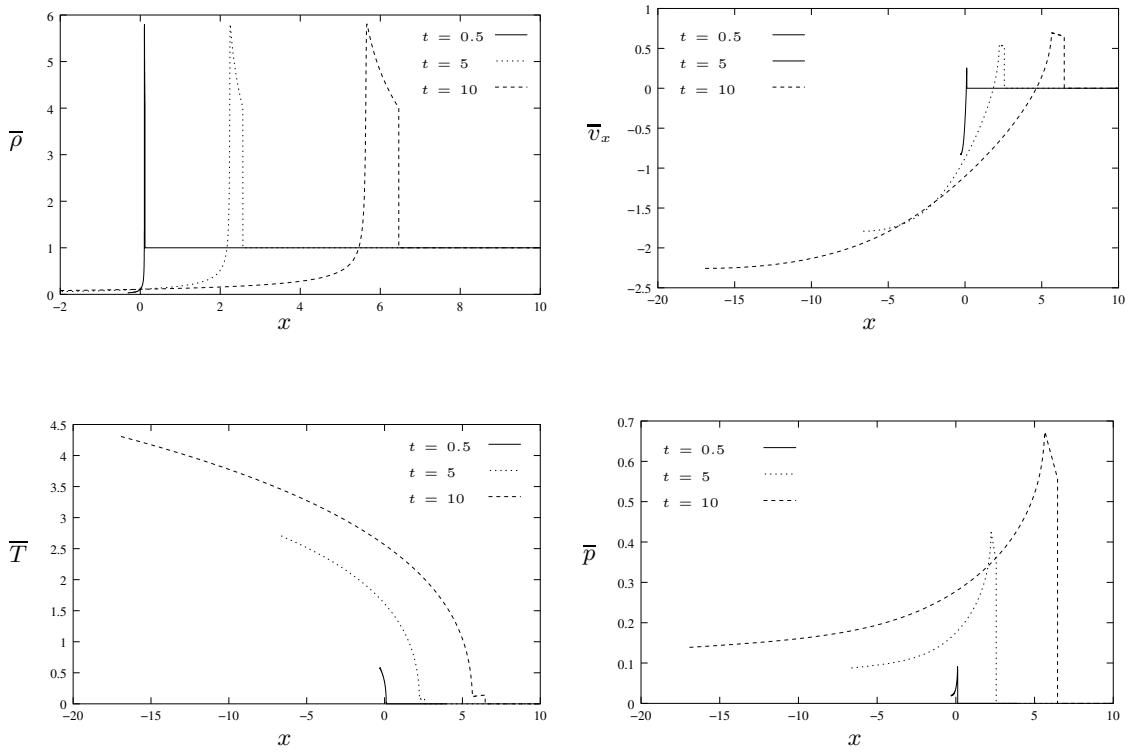

Figure 2: Spatial profiles in the x-variable of the density (top left), velocity (top right), temperature (bottom left) and pressure (bottom right) at times $t = 0.5$, $t = 5$, $t = 10$ for configuration I of Table 1.

3 PERTURBED FLOW

3.1 EQUATIONS AND BOUNDARY CONDITIONS

The equations for the linear perturbations are written using an Eulerian description in the frame of the unperturbed motion. The linear system of equations satisfied by the perturbations, in the coordinate system (m, y, z), is the

following

$$\frac{\partial \rho}{\partial t} + \overline{\rho}^2 \frac{\partial v_x}{\partial m} + \overline{\rho}\left(\frac{\partial \overline{v}_x}{\partial m}\rho + \frac{\partial \overline{\rho}}{\partial m} v_x + \nabla_\perp . \vec{v}_\perp\right) = 0, \tag{25a}$$

$$\frac{\partial v_x}{\partial t} + \frac{\partial p}{\partial m} - \frac{1}{\overline{\rho}}\frac{\partial \overline{p}}{\partial m}\rho + \overline{\rho}\frac{\partial \overline{v}_x}{\partial m} v_x = 0, \tag{25b}$$

$$\frac{\partial \vec{v}_\perp}{\partial t} + \frac{1}{\overline{\rho}}\nabla_\perp p = \vec{0}, \tag{25c}$$

$$\begin{aligned}\frac{\partial \mathcal{E}}{\partial t} + \overline{\rho} v_x \frac{\partial \overline{\mathcal{E}}}{\partial m} = -p\frac{\partial \overline{v}_x}{\partial m} + \overline{p}\left(\frac{\rho}{\overline{\rho}}\frac{\partial \overline{v}_x}{\partial m} - \frac{\partial v_x}{\partial m}\right) \\ + \frac{\rho}{\overline{\rho}}\frac{\partial \overline{\varphi}_x}{\partial m} - \frac{\partial \varphi_x}{\partial m} - \frac{\overline{p}}{\overline{\rho}}\nabla_\perp . \vec{v}_\perp - \frac{1}{\overline{\rho}}\nabla_\perp . \vec{\varphi}_\perp .\end{aligned} \tag{25d}$$

In addition to these equations, the expressions for the heat flux linear perturbations are given by

$$\begin{aligned}\varphi_x &= -\overline{\rho}^{1+\mu}\,\overline{T}^{\nu}\left[\frac{\partial T}{\partial m} + \left((1+\mu)\frac{\rho}{\overline{\rho}} + \nu\frac{T}{\overline{T}}\right)\frac{\partial \overline{T}}{\partial m}\right], \\ \vec{\varphi}_\perp &= -\overline{\rho}^{\mu}\,\overline{T}^{\nu}\nabla_\perp T.\end{aligned} \tag{26}$$

As is usual, the unknown $\vec{v}_\perp$ is replaced by its divergence $\nabla_\perp . \vec{v}_\perp$. By considering the Fourier transforms, in the y- and z-variables, of the above equations, the resulting system comes as (25a, 25b, 25d) along with

$$\partial_t\left(\nabla_\perp . \vec{v}_\perp\right) - k_\perp^2\, p/\overline{\rho} = 0, \text{ with } k_\perp = \sqrt{k_y^2 + k_z^2}, \tag{27}$$

where the same notation has been used for a quantity and its Fourier transform. This system (25a, 25b, 27, 25d) is incompletely parabolic, and well-posed for the Cauchy problem [44].

At the origin ($m = 0$), we impose the perturbed density to be zero, and consider a time-dependent incoming heat-flux perturbation—a choice motivated by laser imprint problems. The first of these two boundary conditions is written as

$$\rho_+ + \eta\ \partial_m \overline{\rho}|_+\ \overline{\rho}_+ = 0, \tag{28}$$

where $\eta(k_\perp, t)$ denotes the amplitude perturbation Fourier component of the perturbed material surface $m = 0$ of equation $x = \eta(y, z, t)$, and $\overline{\rho}|_+$, $\rho|_+$ stand for the limiting values of ρ and $\overline{\rho}$, as $m \to 0^+$. The second boundary condition amounts to the equation

$$\varphi_{x-} = -\overline{\rho}_+^{\,1+\mu}\overline{T}_+^{\,\nu}\ \partial_m T|_+ - \overline{\rho}_+\eta\ \partial_m \overline{\varphi}_x|_+ + \left((1+\mu)\frac{\rho_+}{\overline{\rho}_+} + \nu\frac{T_+}{\overline{T}_+}\right)\overline{\varphi}_x|_+ . \tag{29}$$

At the location of the shock wave, the Rankine-Hugoniot relations for linear perturbations are applied.

3.2 NUMERICAL METHOD

System (25) is solved in the coordinate system (ξ, y, z), where $\xi = m/t^\alpha$. Numerical approximation, in the ξ-variable, is carried out with the same multidomain collocation spectral method as that used for the mean flow. Time integration is performed by using a time-splitting method approach. We decompose the system of PDEs into, a first order hyperbolic system and a second order parabolic equation. Boundary conditions are then spread over these two systems. This splitting is implemented at each step of a three step second-order semi-implicit Runge-Kutta scheme. The hyperbolic system is integrated using the explicit part of this scheme, while the complete scheme is used for the parabolic system.

Hyperbolic system

The hyperbolic system which results from omitting the heat-flux perturbation contribution in (25) reads, in vector form,

$$\frac{\partial \mathbf{V}}{\partial t} + \mathbf{A}_\xi \frac{\partial \mathbf{V}}{\partial \xi} + \mathbf{B}_\xi \mathbf{V} = \mathbf{0}, \tag{30}$$

where $\mathbf{A}_\xi$ and $\mathbf{B}_\xi$ contain coefficients which are functions of t and ξ and the vector of unknowns is $\mathbf{V} = (G\ V_x\ \nabla_\perp.\vec{V}_\perp\ P)^\top$, with the convention

$$\begin{aligned} G(\xi,\, t,\, k_\perp) &= \rho(m,\, t,\, k_\perp), \\ V_x(\xi,\, t,\, k_\perp) &= v_x(m,\, t,\, k_\perp), \\ \nabla_\perp.\vec{V}_\perp(\xi,\, t,\, k_\perp) &= \nabla_\perp.\vec{v}_\perp(m,\, t,\, k_\perp), \\ P(\xi,\, t,\, k_\perp) &= p(m,\, t,\, k_\perp). \end{aligned} \tag{31}$$

Numerical treatments of time-dependent boundary conditions and of subdomain interface matching conditions [45] are based on the method of characteristics along the lines proposed by Thompson and Kopriva [46, 47].

Parabolic equation

The parabolic equation for the temperature is obtained by keeping only the first term and the heat-flux perturbation contribution in (25d)

$$\begin{aligned} \frac{1}{\gamma-1}\left(\frac{\partial}{\partial t} - \alpha\xi t^{-1}\frac{\partial}{\partial\xi}\right)\Theta = {} & t^{-1}\overline{G}^{\mu+1}\overline{\Theta}^{\nu}\,\frac{\partial^2}{\partial\xi^2}\Theta - t^{2\alpha-1}\,k_\perp^2\,\overline{G}^{\mu-1}\,\overline{\Theta}^{\nu}\,\Theta \\ & - t^{2\alpha-3}(\mu+1)\,\frac{\partial}{\partial\xi}\left(\frac{\overline{\Phi}_x\,G}{\overline{G}}\right) \\ & - t^{-1}\left[\nu\,\frac{\mathrm{d}}{\mathrm{d}\xi}\left(\frac{\overline{\Phi}_x}{\overline{\Theta}}\right)\right. \\ & \left. + \left(2\nu\frac{\overline{\Phi}_x}{\overline{\Theta}} - (\mu+1)\,\overline{G}^{\mu}\,\overline{\Theta}^{\nu}\,\frac{\mathrm{d}}{\mathrm{d}\xi}\,\overline{G}\right)\frac{\partial}{\partial\xi}\right]\Theta. \end{aligned} \tag{32}$$

This parabolic equation is handled by an iterative procedure with a second-order finite difference preconditioning. Matching of quantities at subdomain interfaces are carried out with the influence matrix technique [48].

3.3 RESULTS

Laser nonuniformities and target surface roughness are the two major sources of perturbation growth in ICF pellet implosions. Here, we only consider nonuniform laser ablation induced by nonuniform laser irradiation of a smooth target. The flux perturbation, imposed at the boundary $\xi = 0$—equivalent to the energy deposition surface—, is taken to be the following

$$\varphi_x(\xi=0,\, t) \,=\, \overline{\varphi}_x(m=0,\, t)\,\Pi_\varphi(t;\theta) \,\equiv\, t\,\mathcal{B}_\varphi\,\Pi_\varphi(t;\theta) \quad \text{with} \quad \Pi_\varphi(t;\theta) \,=\, \left[1 - 2\,(1+\exp\theta(t-t_\mathrm{i}))^{-1}\right], \tag{33}$$

where t_i is the simulation starting time and θ is a free parameter controlling the rise of the heat-flux perturbation. Computations have been performed for configuration I with $t_\mathrm{i} = 0.1$ and $\theta = 6$ for each of the following transverse wavenumber values: $k_\perp = 0$, 10^{-4}, 10^{-3}, 10^{-2}, 10^{-1}, 0.5, 1, 2, 3, 5, 7, 10, 25, 50, 100.
The ranges covered by the perturbation values (like entropy or vorticity) are particularly large and we sometimes had to use the transformational function $\widetilde{X} = \mathrm{sign}(X)\log_{10}(1 + 1000\,|X|)$ in the graphical representations involving these quantities.

3.3.1 "AMPLIFICATION SHEET"

Almost all perturbations have local extrema in the vicinity of the ablation front. Time evolutions of the magnitude of such extrema for the density perturbation $\max_\xi|G|(t,\, k_\perp)$ are shown for all wavenumbers considered here in Fig. 3. The resulting set of curves constitutes what we call the *amplification sheet* of the density perturbation. For small values of the transverse wavenumbers $k_\perp$, after a period of pure growth, the quantity $\max_\xi|G|(t,\, k_\perp)$ stays nearly constant. For increasing values of $k_\perp$, the duration of the growth period shortens as a transient attenuation regim sets in, itself followed by a persisting oscillatory regime of smaller amplitudes. A noticeable

feature of this amplification sheet is that its maximum level is reached for $k_\perp = 0$. By appropriately choosing a level curve $\max_\xi |G|(t,\, k_\perp) = \text{cst}$ on this amplification sheet, we may identify the transient attenuation regime in the $(\log t,\, \log k_\perp)$-plane (see Fig. 4). In this plane, the corresponding level curve follows approximately a straight

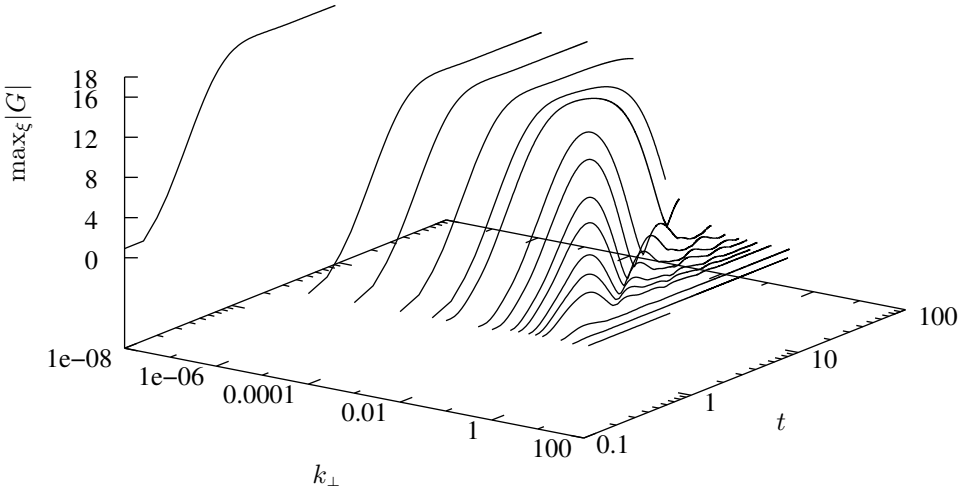

Figure 3: Density perturbation amplification sheet for $10^{-8} \leq k_\perp \leq 10^2$ and $0.1 \leq t \leq 15$.

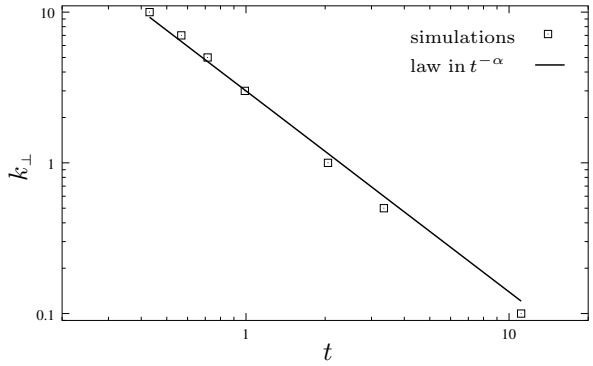

Figure 4: Level curve $\max_\xi |G| = 1$ in the plane $(\log t,\, \log k_\perp)$.

line of slope $-4/3$, *i. e.*, given by the similarity exponent α. The fact that this exponent is entirely determined by the temperature exponent ν of the thermal conductivity strongly suggests that the damping of perturbations at the ablation front is governed by thermal diffusion. Let us emphasize that the small amplitude oscillatory regimes seem to persist even for increasing wavenumbers.

3.3.2 WAVE-LIKE STRUCTURES

In this section, we restrict ourselves to a qualitative description of the wave structures revealed by the numerical simulations.

Behaviour of the perturbed ablation front

The temporal evolution of the location of the density perturbation extrema is shown in Fig. 5. For a transverse wavenumber $k_\perp = 10^{-3}$, the extremum rapidly tends to a fixed abscissa, while for $k_\perp = 50$, this extremum oscillates about a mean value.

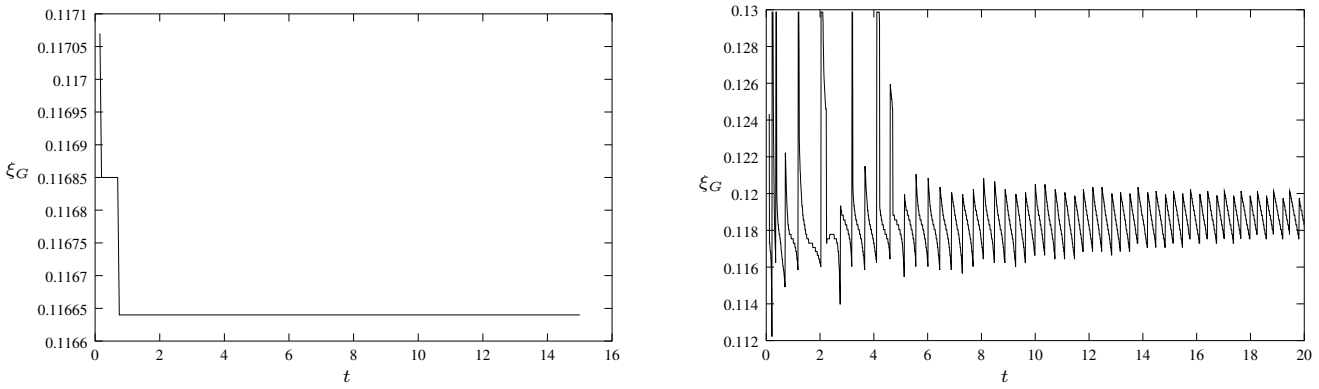

Figure 5: Temporal evolution of the location of $\max_\xi |G|$ for $k_\perp = 10^{-3}$ (left) and $k_\perp = 50$ (right).

Early time behaviour

The early time behaviour of the density perturbation is represented in Fig. 6 for two transverse wavenumbers, $k_\perp = 10^{-3}$ (left) and $k_\perp = 50$ (right). For these two wavenumbers, and for all the others, the density perturbation is rapidly amplified at the ablation front and propagates from the ablation front towards the shock-wave front at the same group velocity.

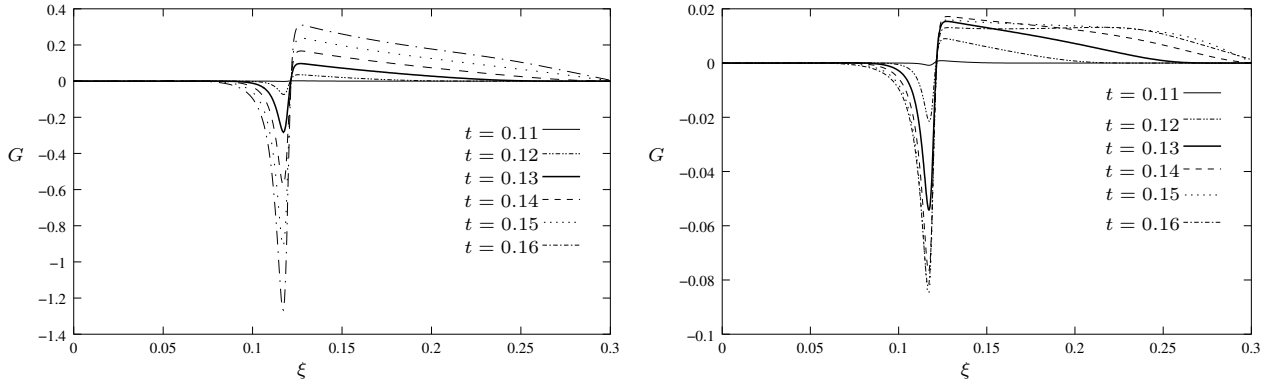

Figure 6: Early time behaviour of the density perturbation for wavenumbers $k_\perp = 10^{-3}$ and $k_\perp = 50$ for $0.11 \leq t \leq 0.16$.

Space-time structures of Kovásznay modes

The three Kovásznay modes [49], namely, the pressure, entropy and vorticity which have been transformed with the function $\widetilde{X}$ are shown in Figures 7 and 8 in the space (m, t) for wavenumbers $k_\perp = 10^{-3}$ and $k_\perp = 50$, respectively. In the Lagrangian variable m, the shock-wave front and the ablation front are clearly visible. The perturbations are significantly amplified as they cross the ablation front, this behaviour is especially visible for wavenumber $k_\perp = 10^{-3}$. The plots of $\widetilde{P}$, $\widetilde{S}$, $\widetilde{\Omega}$ display plateau-like regions for wavenumber $k_\perp = 10^{-3}$, whereas for wavenumber $k_\perp = 50$, spatial structures appear in the compressed region. In the compressed region, acoustic waves propagate and we observe the multiple acoustic interactions between the shock-wave front and the ablation front. Note that the vorticity perturbation appears stationary in this same region, indicating that it is simply convected by the mean flow downstream of the shock front. In contrast to the other two quantities, the vorticity perturbation is weakly damped in the heat-conduction region. Near the origin, the flow expands supersonically and the three modes, pressure, entropy and vorticity waves are trapped in this region—dark zones close to the origin on the plots of Fig. 8 are characteristic of this trapping.

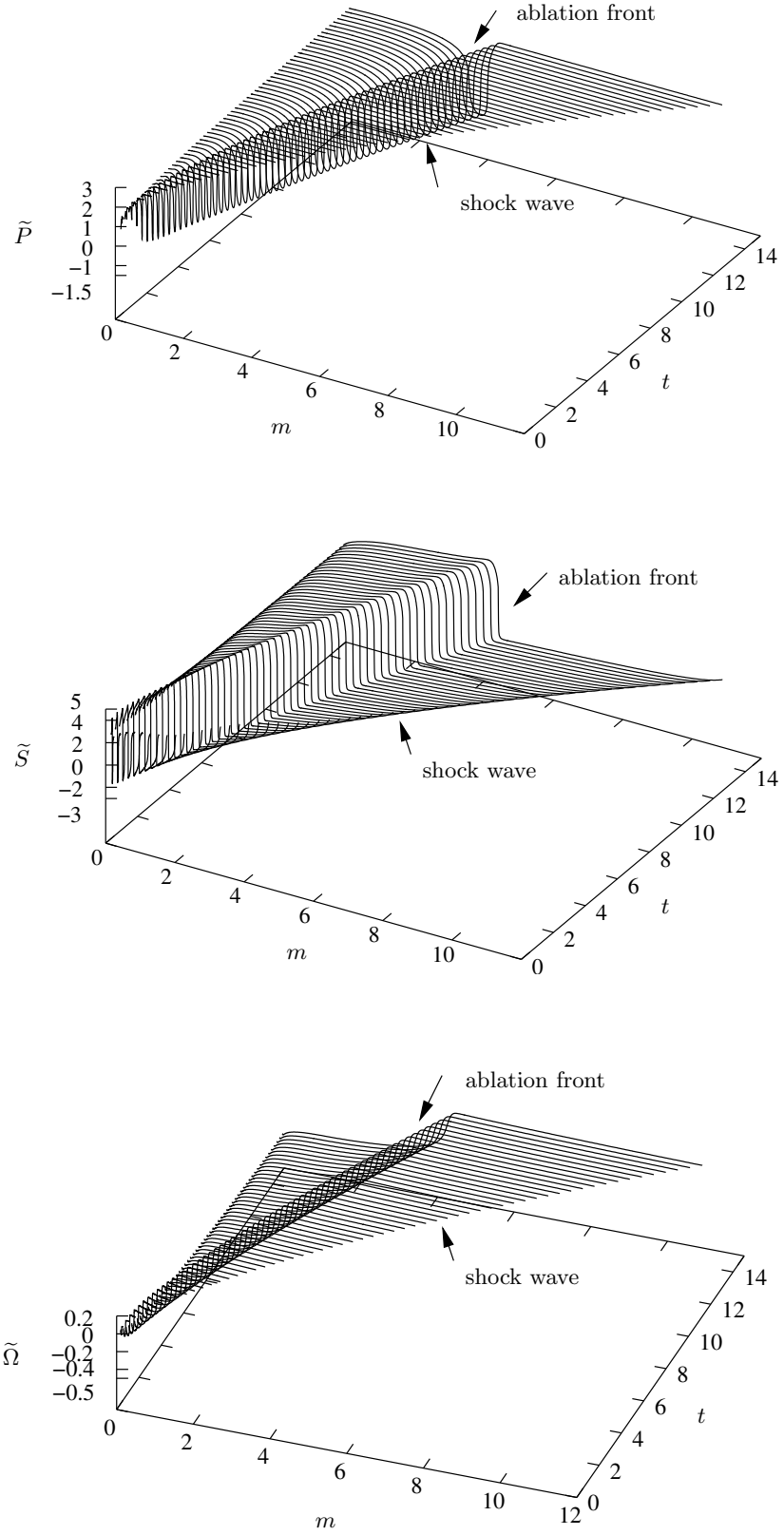

Figure 7: Transformed pressure $\widetilde{P}$ (top), entropy $\widetilde{S}$ (middle) and vorticity $\widetilde{\Omega}$ (bottom) perturbations as functions of (m, t) for wavenumber $k_\perp = 10^{-3}$ and for the domain $0 \le m \le 12$, $0.1 \le t \le 15$.

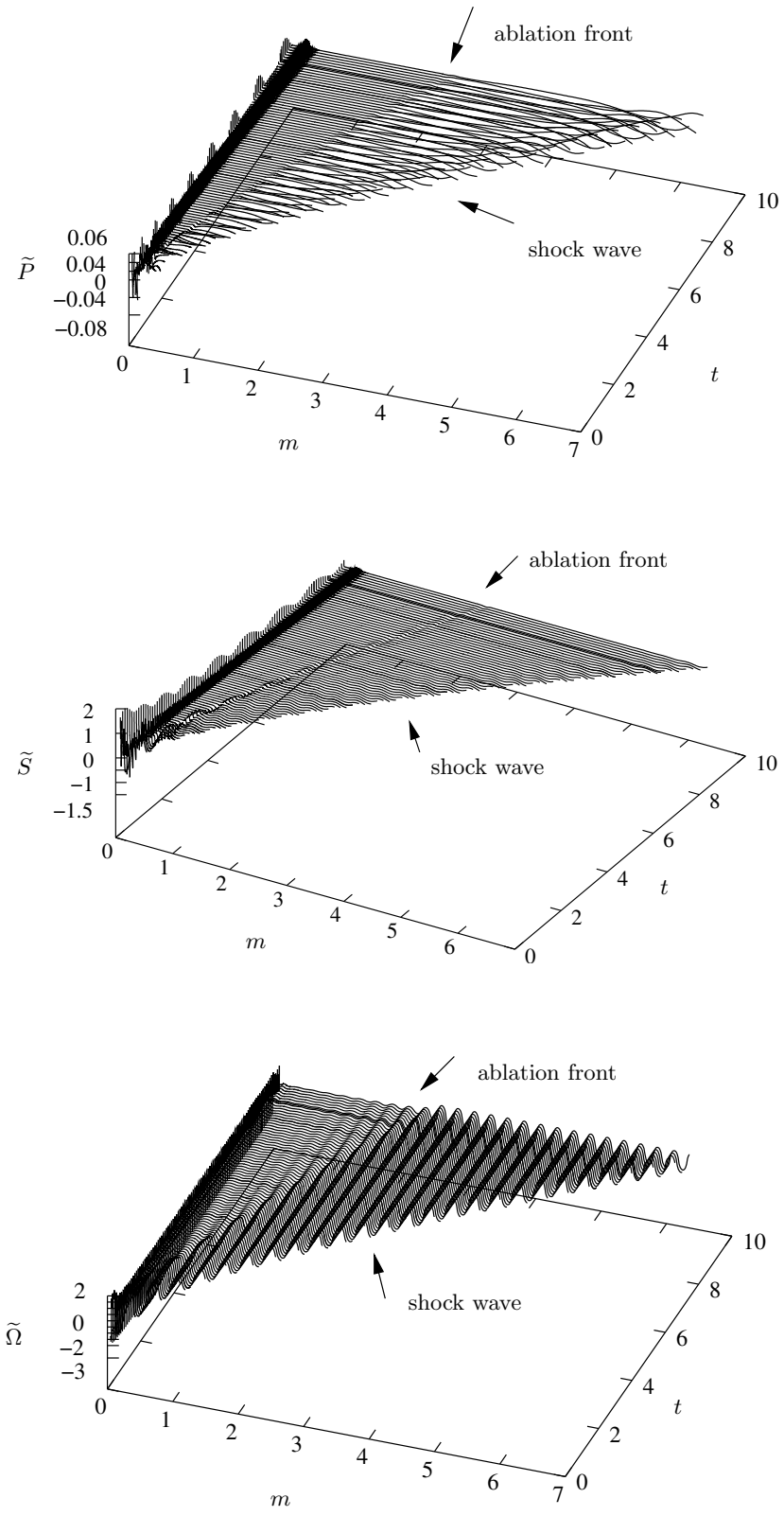

Figure 8: Transformed pressure $\widetilde{P}$ (top), entropy $\widetilde{S}$ (middle) and vorticity $\widetilde{\Omega}$ (bottom) perturbations as functions of (m, t) for wavenumber $k_\perp = 50$ and for the domain $0 \leq m \leq 7$, $0.1 \leq t \leq 10$.

Time behaviour of perturbations at the shock wave location

Density perturbation time evolutions at the shock-wave front are displayed in Fig. 9 for wavenumber $k_\perp = 10^{-3}$ and in Fig. 10 for wavenumber $k_\perp = 50$. The evolution for wavenumber $k_\perp = 10^{-3}$ exhibits two regimes: a rapid growth of the perturbation amplitude followed by a nearly constant regime. The evolution for wavenumber $k_\perp = 50$ displays three phases: a growth phase, a damped oscillatory phase and a modulated oscillatory phase. This last behaviour is different from that of an isolated perturbation shock-wave travelling at a constant velocity.

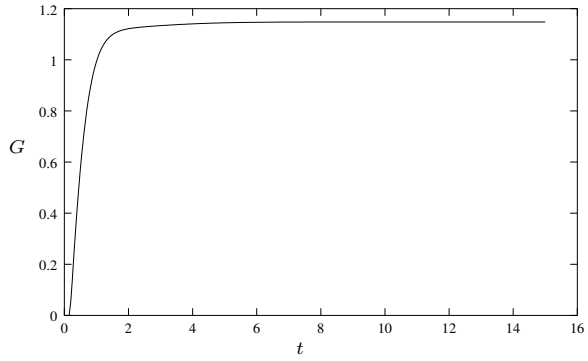

Figure 9: Density perturbation time evolutions at the shock-wave front for wavenumber $k_\perp = 10^{-3}$ and for $0.1 \leq t \leq 15$.

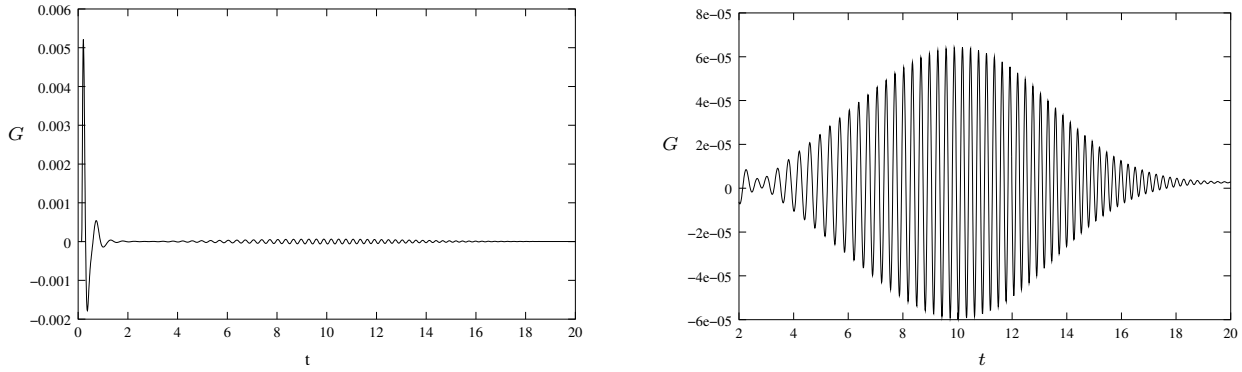

Figure 10: Density perturbation time evolutions at the shock-wave front for wavenumber $k_\perp = 50$, for $0.1 \leq t \leq 20$ (left) and for $2 \leq t \leq 20$ (right).

4 CONCLUDING REMARKS

In this paper, we have presented realistic self-similar ablation flows obtained with a high accuracy and results of the linear stability analysis for one of them. The main findings of this paper are that:

- maximum perturbation amplitudes in the thin ablation front layer are reached for transverse wavenumber $k_\perp = 0$;
- the damping of ablation front perturbations is closely related to thermal diffusion;
- ablation front perturbations seem to persist for increasing transverse wavenumbers.

The preliminary analysis of the wave-like structures seems to exhibit two different regimes: a steady regime at very low wavenumbers (see Fig. 5 (left), Fig. 6 (left), Fig. 7 and Fig. 9) and an oscillatory regime for large wavenumbers (see Fig. 5 (right), Fig. 6 (right), Fig. 8 and Fig. 10). Further analyses are required to understand more clearly these behaviours.

Acknowledgments

The authors wish to acknowledge Dr. L. Hallo (CEA) and Prof. R. Betti (University of Rochester) for stimulating discussions and Dr. X. Fortin for providing numerical simulations data corresponding to Mégajoule laser conditions. F.A. wishes to thank Prof. R. Gatignol (Université Paris 6) for providing hospitality and support during his PhD. thesis at LMM (Université Paris 6), where a major part of this work has been completed. Computations of the present paper have been performed on the high performance computing facilities at CCR (Université Paris 6).

References

[1] C. Boudesocque-Dubois. *Perturbations linéaires d'une solution autosemblable de l'hydrodynamique avec conduction non linéaire*. Thèse de doctorat, Université de Paris 6, 2000.

[2] C. Boudesocque-Dubois, J.-M. Clarisse, and S. Gauthier. Hydrodynamic stability of ablation fronts: linear perturbation of a self-similar solution. *Bull. Amer. Phys. Soc.*, 45(7):198–199, 2000.

[3] F. Abéguilé. *Étude de l'instabilité hydrodynamique d'écoulements autosemblables d'ablation*. Thèse de doctorat, Université de Paris 6, 2004.

[4] L. Sedov. *Similarity and dimensional methods in mechanics*. Academic Press, New-York, 1959.

[5] Ya. B. Zel'dovich and Yu. P. Raizer. *Physics of shock waves and high-temperature hydrodynamic phenomena*. Academic Press, 1967.

[6] G. I. Barenblatt. *Similarity, self-similarity, and intermediate asymptotics*. Consultants Bureau, New-York, 1979.

[7] D. S. Butler. Stability of converging cylindrical and spherical shock waves. Technical Report 18/56, A. R. D. E. Report, 1956.

[8] D. L. Book and I. B. Bernstein. Fluid instabilities of a uniformly imploding ablatively driven shell. *J. Plasma Physics*, 23(3):521–533, 1980.

[9] J. Lindl, P. Amendt, R. Berger, S. Glendinning, S. Glenzer, S. Haan, R. Kauffman, O. Landen, and L. Suter. The physics basis for ignition using indirect-drive targets on the National Ignition Facility. *Phys. Plasmas*, 11(2):339–491, 2004.

[10] S.E. Bodner. Rayleigh-Taylor instability and laser-pellet fusion. *Phys. Rev. Lett.*, 33(11):761–764, 1974.

[11] K. A. Brueckner and S. Jorna. Laser-driven fusion. *Reviews of Modern Physics*, 46(2):325–367, 1974.

[12] J. D. Lindl and W. C. Mead. Two-dimensional simulation of fluid instability in laser-fusion pellets. *Phys. Rev. Lett.*, 34(20):1273–1276, 1975.

[13] W. M. Manheimer and D. G. Colombant. Slab model for Rayleigh-Taylor stabilization by vortex shedding, compressibility, thermal conduction, and ablation. *Phys. Fluids*, 27(4):983–993, 1984.

[14] H.J. Kull and S.I. Anisimov. Ablative stabilization in the incompressible Rayleigh-Taylor instability. *Phys. Fluids B*, 7:2067–2075, 1986.

[15] H.J. Kull. Incompressible description of Rayleigh-Taylor instabilities in laser-ablated plasmas. *Phys. Fluids B*, 1(1):170–182, 1989.

[16] V.V. Bychkov, S.M. Golberg, and M.A. Libermann. Growth rate of the Rayleigh-Taylor instability in an ablatively accelerated inhomogeneous laser plasma. *Sov. Phys. JETP*, 73(4):642–653, 1991.

[17] J. Sanz. Self-consistent analytical model of the Rayleigh-Taylor instability in inertial confinement fusion. *Phys. Rev. Lett.*, 73(20):2700–2703, 1994.

[18] J. Sanz. Self-consistent analytical model of the Rayleigh-Taylor instability in inertial confinement fusion. *Phys. Rev. E*, 53(4):4026–4045, 1996.

[19] R. Betti, V.N. Goncharov, R.L. McCrory, and C.P. Verdon. Self-consistent cutoff wave number of the ablative Rayleigh-Taylor instability. *Phys. Plasmas*, 2(10):3844–3851, 1995.

[20] J.G. Wouchuk and A.R. Piriz. Growth rate reduction of the Rayleigh-Taylor instability by ablative convection. *Phys. Plasmas*, 2(2):493–500, 1995.

[21] V.N. Goncharov, R. Betti, R.L. McCrory, P. Sorotokin, and C.P. Verdon. Self-consistent stability analysis of ablation fronts with large Froude numbers. *Phys. Plasmas*, 3(4):1402–1414, 1996.

[22] V.N. Goncharov, R. Betti, R.L. McCrory, and C.P. Verdon. Self-consistent stability analysis of ablation fronts with small Froude numbers. *Phys. Plasmas*, 3(12):4665–4676, 1996.

[23] A. R. Piriz, J. Sanz, and L. F. Ibanez. Rayleigh-Taylor instability of steady ablation fronts: The discontinuity model revisited. *Phys. Plasmas*, 4(4):1117–1126, 1997.

[24] A. L. Velikovich, J. P. Dahlburg, J. H. Gardner, and R. J. Taylor. Saturation of perturbation growth in ablatively driven planar laser targets. *Phys. Plasmas*, 5(5):1491–1505, 1998.

[25] R. Ishizaki and K. Nishihara. Propagation of a rippled shock wave driven by nonuniform laser ablation. *Phys. Rev. Lett.*, 78(10):1920–1923, 1997.

[26] R. J. Taylor, A. L. Velikovich, J. P. Dahlburg, and J. H. Gardner. Saturation of laser imprint on ablatively driven plastic targets. *Phys. Rev. Lett.*, 79(10):1861–1864, 1997.

[27] V. N. Goncharov. Theory of the ablative Richtmyer-Meshkov instability. *Phys. Rev. Lett.*, 82(10):2091–2094, 1999.

[28] V. N. Goncharov, S. Skupsky, T. R. Boehly, J. P. Knauer, P. McKenty, V. A. Smalyuk, R. P. Town, O. V. Gotchev, R. Betti, and D. D. Meyerhofer. A model of laser imprinting. *Phys. Plasmas*, 7(5):2062–2068, 2000.

[29] R. Marshak. Effect of radiation on shock wave behavior. *Phys. Fluids*, 1(1):24–29, 1958.

[30] S. I. Anisimov. Self-similar thermal wave in a two-temperature plasma heated by a laser pulse. *JETP Lett.*, 12:287–289, 1970.

[31] L. Brun, R. Dautray, F. Delobeau, C. Patou, F. Perrot, J.-M. Reisse, B. Sitt, and J.-P. Watteau. Physical models and mathematical simulation of laser-driven implosion and their relations with experiments. In H. J. Schwarz and H. Hora, editors, *Laser interaction and related plasma phenomena*, volume 4B, pages 1059–1080. Plenum Publising Corp., 1977.

[32] A. Barrero and J.R. Sanmartin. Self-similar motion of laser fusion plasmas. Absorption in an unbounded plasma. *Phys. Fluids*, 20(7):1155–1163, 1977.

[33] J.R. Sanmartin and A. Barrero. Self-similar motion of laser half-space plasmas. I. Deflagration regimes. *Phys. Fluids*, 21(11):1957–1966, 1978.

[34] J.R. Sanmartin and A. Barrero. Self-similar motion of laser half-space plasmas. II. Thermal wave and intermediate regimes. *Phys. Fluids*, 21(11):1967–1971, 1978.

[35] Y. Saillard. Solutions exactes de l'ablation induite par une onde thermique. Internal report, CEA, 1983.

[36] J. Sanz, A. R. Piriz, and F. G. Tomasel. Self-similar model for tamped ablation driven by thermal radiation. *Phys. Fluids B*, 4(3):683–692, 1992.

[37] C. Boudesocque-Dubois, J.-M. Clarisse, and S. Gauthier. Hydrodynamic stability of ablation fronts: linear perturbation of a self-similar solution. In M. Kálal, K. Rohlena, M. Šiňor, editor, *ECLIM: 26th European Conference on Laser Interaction with Matter*, volume 4424, pages 220–223. SPIE, 2001.

[38] L. D. Landau and E. M. Lifchitz. *Fluid Mechanics*. Pergamon New-York, 1987.

[39] R. Peyret. *Spectral methods for incompressible fluids*. Springer-Verlag, New-York, 2002.

[40] H. Guillard, J.-M. Malé and R. Peyret. Adaptive spectral methods with application to mixing layer computations. *J. Comput. Phys.*, 102:114–127, 1992.

[41] F. Renaud and S. Gauthier. A dynamical pseudo-spectral domain decomposition technique: Application to viscous compressible flows. *J. Comput. Phys.*, 131:89–108, 1997.

[42] S. Gauthier. A spectral collocation method for two-dimensional compressible convection. *J. Comput. Phys.*, 75:217–235, 1988.

[43] E. G. Gamalĩi, V. B. Rozanov, A. A. Samarskĩi, V. F. Tishkin, N. N. Tyurina and A. P. Favorskĩi. Hydrodynamic stability of compression spherical laser targets. *Sov. Phys. JETP*, 52(2):230–237, 1980.

[44] B. Gustafsson and Sundström. Incompletely parabolic problems in fluid dynamics. *Siam J. Appl. Math.*, 35:343–357, 1978.

[45] C. Boudesocque-Dubois, J.-M. Clarisse and S. Gauthier. A spectral Chebyshev method for linear stability analysis of one-dimensional exact solutions of gas dynamics. *J. Comput. Phys.*, 184:592–618, 2003.

[46] K. Thompson. Time dependent boundary conditions for hyperbolic systems, II. *J. Comput. Phys.*, 89:439–461, 1990.

[47] D.A. Kopriva. A spectral multidomain method for the solution of hyperbolic systems. *Appl. Numer. Math.*, 2:221–241, 1986.

[48] J.-P. Pulicani. A spectral multi-domain method for the solution of 1D-Helmholtz and Stokes-type equations. *Computers and Fluids*, 16:207–215, 1988.

[49] B.T. Chu and L.S.G. Kovàsznay. Non-linear interactions in a viscous heat-conducting compressible gas. *J. Fluid Mech.*, 3:494–514, 1958.